

Reviving MeV-GeV Indirect Detection with Inelastic Dark Matter

Asher Berlin^{a,b,*}, Gordan Krnjaic^{a,c,d,†} and Elena Pinetti^{a,d,‡}

^a*Theory Division, Fermi National Accelerator Laboratory*

^b*Superconducting Quantum Materials and Systems Center (SQMS), Fermi National Accelerator Laboratory*

^c*University of Chicago, Department of Astronomy and Astrophysics and*

^d*University of Chicago, Kavli Institute for Cosmological Physics*

Thermal relic dark matter below ~ 10 GeV is excluded by cosmic microwave background data if its annihilation to visible particles is unsuppressed near the epoch of recombination. Usual model-building measures to avoid this bound involve kinematically suppressing the annihilation rate in the low-velocity limit, thereby yielding dim prospects for indirect detection signatures at late times. In this work, we investigate a class of cosmologically-viable sub-GeV thermal relics with late-time annihilation rates that are detectable with existing and proposed telescopes across a wide range of parameter space. We study a representative model of inelastic dark matter featuring a stable state χ_1 and a slightly heavier excited state χ_2 whose abundance is thermally depleted before recombination. Since the kinetic energy of dark matter in the Milky Way is much larger than it is during recombination, $\chi_1\chi_1 \rightarrow \chi_2\chi_2$ upscattering can efficiently regenerate a cosmologically long-lived Galactic population of χ_2 , whose subsequent coannihilations with χ_1 give rise to observable gamma-rays in the ~ 1 MeV – 100 MeV energy range. We find that proposed MeV gamma-ray telescopes, such as e-ASTROGAM, AMEGO, and MAST, would be sensitive to much of the thermal relic parameter space in this class of models and thereby enable both discovery and model discrimination in the event of a signal at accelerator or direct detection experiments.

I. INTRODUCTION

Light dark matter (DM) has received much attention over the past decade as new terrestrial experiments have been proposed to vastly expand laboratory sensitivity to new physics below the electroweak scale – for reviews, see Refs. [1, 2]. Amongst the various possibilities, MeV–GeV scale DM in the form of a light thermal relic is especially motivated by basic principles of early-Universe thermodynamics and known examples within the Standard Model (SM) [3].

Thermal DM is in equilibrium with the visible sector at early times and later freezes out after becoming non-relativistic, such that number-changing reactions occur less than once per Hubble time. Although such reactions remain out of equilibrium, rare annihilation events can continue to inject energy into the SM plasma. For instance, DM annihilations into electromagnetically-charged particles can persist between recombination and reionization, yielding observable distortions in the temperature anisotropies of the cosmic microwave background (CMB). The lack of such deviations sharply constrains some of the most predictive and well-motivated freeze-out models [4, 5]. This limit can be phrased in terms of the thermally-averaged annihilation cross section $\langle\sigma v\rangle$ to visible states, which at the time of recombination is constrained by the Planck satellite at the level

of [6]

$$\langle\sigma v\rangle_{\text{cmb}} \lesssim 3 \times 10^{-26} \text{ cm}^3 \text{ s}^{-1} \left(\frac{m_{\text{DM}}}{10 \text{ GeV}} \right), \quad (1)$$

where m_{DM} is the DM mass. Since standard thermal DM predicts $\langle\sigma v\rangle \sim 10^{-26} \text{ cm}^3 \text{ s}^{-1}$ at the time of freeze-out when the DM was quasi-relativistic, models involving annihilations to visible final states with velocity-independent (*s*-wave) cross sections are excluded for masses below ~ 10 GeV.

Of course, this cross section needs not be velocity-independent, and the CMB bound is naturally evaded in models where the annihilation rate is suppressed by the small DM velocity v during recombination. For example, in models with *p*-wave annihilation, $\langle\sigma v\rangle \propto v^2$, so that this rate is significantly smaller at later times when DM is highly non-relativistic. However, this approach¹ also severely diminishes the prospects for indirect detection in the Galaxy, since the local annihilation rate is suppressed by the small virial velocity $v \sim 10^{-3}$, resulting in $\sigma v < 10^{-30} \text{ cm}^3 \text{ s}^{-1}$ for standard thermal relics. Since such small cross sections are beyond the reach of any near-future probe (see Refs. [13, 14] and references therein), there is strong motivation to identify well-motivated and testable targets for indirect detection in the MeV – GeV mass range.

¹ Although larger Galactic annihilation rates can arise in other models of thermal relics involving resonant [7–9] or forbidden annihilations [10–12], this is typically promising only when the relative mass-splitting between various dark sector states is fixed to a special value, corresponding to a strong tuning between mass scales that are related to independent model parameters.

* aberlin@fnal.gov

† krnjaicg@fnal.gov

‡ epinetti@fnal.gov

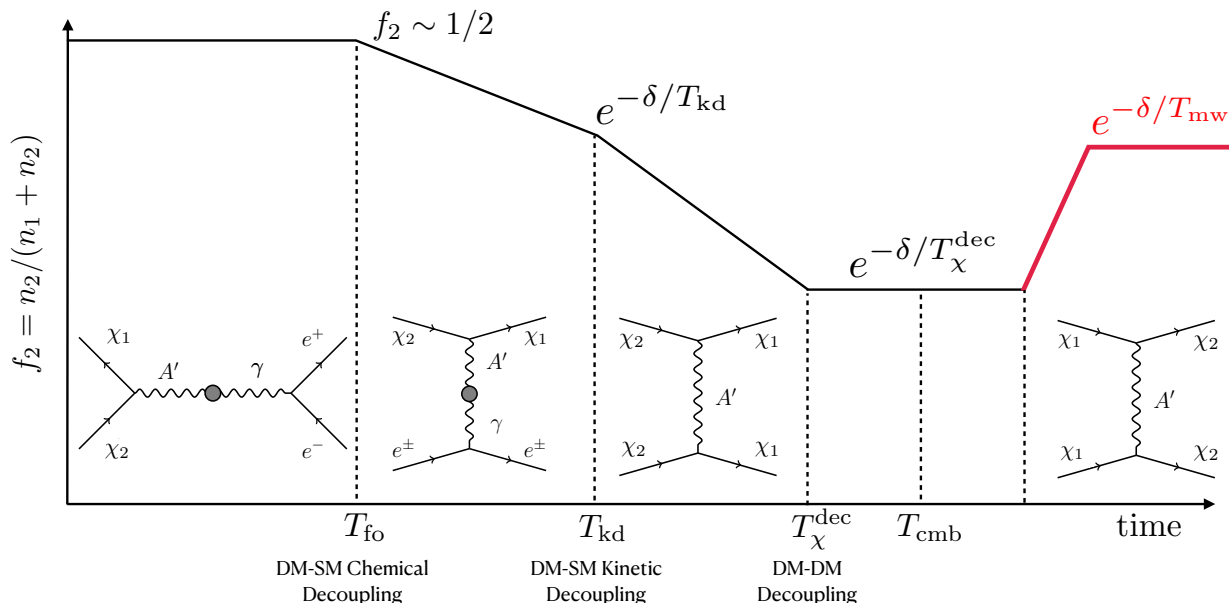


FIG. 1: A timeline of key events in the cosmic history of iDM. At early times, coannihilations $\chi_1\chi_2 \rightarrow \text{SM SM}$ freeze out at a temperature much greater than the mass-splitting $T_{\text{fo}} \gg \delta$, leaving behind roughly equal $\chi_{1,2}$ populations with a χ_2 number fraction $f_2 = n_2/(n_1 + n_2) \simeq 1/2$. After freeze-out, χ_2 continues to be depleted through DM-SM and DM-DM scattering. DM-SM scattering additionally keeps the dark sector in kinetic equilibrium with the SM until decoupling at a temperature of T_{kd} . At later times, the heavier state continues to be depleted more rapidly through $\chi_2\chi_2 \rightarrow \chi_1\chi_1$ downscattering until decoupling at a DM temperature of T_{χ}^{dec} , such that the primordial fraction of excited states is exponentially suppressed at the time of recombination. As a result, CMB limits on DM annihilations are easily evaded. At much later times, the virialization of DM in the Milky Way increases its velocity, such that $\chi_1\chi_1 \rightarrow \chi_2\chi_2$ upscattering partially restores the abundance of long-lived heavier states and enhances the coannihilation rate compared to its average cosmological value (red line). This increase implies a local enhancement of $\chi_1\chi_2 \rightarrow \text{SM SM}$ in the Milky Way whenever the effective Galactic temperature of DM satisfies $T_{\text{mw}} \gtrsim T_{\chi}^{\text{dec}}$. If the χ_2 population becomes appreciable in the Galaxy, then $\chi_1\chi_2 \rightarrow \chi_1\chi_2$ elastic scattering can also play an important role in Galaxy evolution.

An alternative approach to evading the CMB limit on sub-GeV thermal DM involves *changing* the DM population between freeze-out and recombination, as in models of “inelastic DM” (iDM) [15]. In this framework, such evolution occurs dynamically in a dark sector containing a nearly-degenerate pseudo-Dirac DM pair, χ_1 and χ_2 , with a small mass-splitting and an off-diagonal coupling to the SM. The natural size of the mass-splitting is near or below the overall DM mass scale if it arises from the same dynamics responsible for generating the dark sector masses [15–17]. In this case, DM annihilation proceeds efficiently at early times through coannihilations of χ_1 and χ_2 to SM final states, but is exponentially suppressed before recombination as the Universe cools and DM self-scattering continues to thermally deplete the abundance of the heavier χ_2 state in favor of the lighter χ_1 state. A summary of the cosmological history is depicted schematically in Fig. 1.

In this paper, we point out that the kinetic energy of χ_1 in the Milky Way is sufficiently large to undo this exponential suppression at late times and thus regenerate a population of upscattered χ_2 excited states that

are detectable through their subsequent coannihilation to visible states, $\chi_1\chi_2 \rightarrow \text{SM SM}$. In particular, we highlight the existence of cosmologically-viable and theoretically well-motivated parameter space involving mass-splittings of $\sim 1 \text{ eV} - 100 \text{ eV}$, such that the kinetic energy of MeV – GeV scale DM in the Milky Way is sufficient to partially or fully equilibrate a density of cosmologically long-lived excited states. As a result, coannihilations that yield low-energy gamma-rays occur at a rate comparable to (or a few orders of magnitude below) the thermal value for s -wave annihilation, which is detectable with existing and proposed indirect detection searches in the Milky Way. In contrast, analogous signals of such processes are suppressed in the early Universe as well as in less dense astrophysical bodies, such as dwarf satellite galaxies, due to the smaller DM velocities involved.

We note that analogous ideas involving the regeneration of late-time indirect detection signals have been previously explored within the context of prompt decays of excited iDM states [18–20], late-time decays in a multi-component hidden sector [21], and annihilations from asymmetric DM oscillations [22]. While such work

is similar in spirit to our study, these models typically involve additional particle content or early-Universe dynamics compared to the model here. By contrast, we present a simple scenario with standard cosmological assumptions where the same interaction that sets the DM thermal relic abundance is also responsible for indirect detection signals in the Galaxy.

The remainder of this paper is organized as follows. In Secs. II and III, we provide an overview of iDM models and their cosmological history. In Sec. IIID, these results are used to determine the primordial fraction of excited states at late times. In Sec. IV, we study the Galactic dynamics of this scenario and calculate the excited DM population in the Milky Way. These results are then used in Secs. V and VI to derive limits from existing indirect detection searches as well as prospects for observing such a population in low-energy gamma-rays with proposed satellites. Finally, we offer concluding remarks in Sec. VII and discuss directions for future work. A series of appendices, referred to throughout this work, provides additional technical details.

II. MODEL OVERVIEW

In this section, we outline a concrete model of iDM. The DM content of this model involves a Dirac pair of two-component Weyl fermions, ψ_1 and ψ_2 , oppositely charged under a new spontaneously broken $U(1)'$ symmetry with gauge interaction

$$\mathcal{L} \supset e' A'_\mu (\psi_1^\dagger \bar{\sigma}^\mu \psi_1 - \psi_2^\dagger \bar{\sigma}^\mu \psi_2), \quad (2)$$

where the dark photon A' is the $U(1)'$ gauge boson with mass $m_{A'}$ and gauge coupling e' . The fermion masses of this theory arise from the Lagrangian terms

$$\mathcal{L} \supset -m_D \psi_1 \psi_2 - \frac{1}{2} (\delta_1 \psi_1 \psi_1 + \delta_2 \psi_2 \psi_2) + \text{h.c.}, \quad (3)$$

where m_D is a gauge-invariant Dirac mass and $\delta_{1,2}$ are $U(1)'$ breaking Majorana masses naturally² satisfying $\delta_{1,2} \ll m_D$. After diagonalizing this system, the mass eigenstates correspond to a pseudo-Dirac pair,

$$\chi_1 \simeq \frac{i}{\sqrt{2}} (\psi_1 - \psi_2), \quad \chi_2 \simeq \frac{1}{\sqrt{2}} (\psi_1 + \psi_2), \quad (4)$$

with nearly degenerate masses

$$m_{1,2} \simeq m_D \mp \frac{1}{2} (\delta_1 + \delta_2) \quad (5)$$

split by the small amount $\delta \equiv \delta_1 + \delta_2 \ll m_{1,2}$. In terms of mass eigenstates, the leading interaction of Eq. 2 is off-diagonal,

$$\mathcal{L} \supset i e' A'_\mu \bar{\chi}_1 \gamma^\mu \chi_2 + \mathcal{O}\left(\frac{\delta_{1,2}}{m_D}\right), \quad (6)$$

where we have written $\chi_{1,2}$ as four-component Majorana spinors.

Generically, χ_1 and χ_2 also couple diagonally to the A' , but these interactions are suppressed by $\delta/m_1 \ll 1$ and exactly vanish if $\delta_1 = \delta_2$ due to the enhanced charge conjugation symmetry $\chi_{1,2} \rightarrow \mp \chi_{1,2}$, $A' \rightarrow -A'$. Without loss of essential generality, throughout this paper we assume that $\chi_{1,2}$ couple purely off-diagonally to the dark photon, as in Eq. 6, which governs the dynamics within the dark sector. For instance, Eq. 6 facilitates up-scattering $\chi_1 \chi_1 \rightarrow \chi_2 \chi_2$ as well as *elastic* self-scattering $\chi_1 \chi_2 \rightarrow \chi_1 \chi_2$ between DM particles, both of which can have significant impacts on the Galactic population, as we will discuss below.

The dark photon coupling to the electromagnetic current arises from a small kinetic mixing between A' and the SM photon field A ,

$$\mathcal{L} \supset \frac{\epsilon}{2} F'_{\mu\nu} F^{\mu\nu} + A_\mu J_{\text{em}}^\mu, \quad (7)$$

where F' and F are the dark and visible field strengths, respectively, J_{em} is the SM electromagnetic current, and $\epsilon \ll 1$ is the dimensionless parameter governing the strength of A' - A mixing. After rotating away this mixing via $A \rightarrow A + \epsilon A'$, SM fields acquire a small coupling to the dark photon through the induced interaction $\epsilon A'_\mu J_{\text{em}}^\mu$ [23].

III. COSMOLOGICAL HISTORY

In this section, we review the cosmological history of sub-GeV iDM. The discussion is organized into different subsections, ordered chronologically according to when various processes decouple in the early Universe in the parameter space of interest. In particular, we discuss DM – SM chemical decoupling, DM – SM kinetic decoupling, and $\chi_1 - \chi_2$ chemical decoupling, respectively, as depicted in Fig. 1. For previous work investigating such cosmological scenarios, see, e.g., Refs. [24, 25].

A. DM – SM Chemical Decoupling

Here we discuss DM thermal freeze-out, the process of DM – SM chemical decoupling which sets the total $\chi_{1,2}$ density in the early Universe. If the kinetic mixing parameter satisfies

$$\epsilon \gtrsim 10^{-8} \sqrt{\frac{m_{A'}}{\text{GeV}}}, \quad (8)$$

² Indeed, the Majorana terms are small if they arise from higher-dimensional couplings to the dark Higgs H' responsible for spontaneous breaking in the dark sector (e.g., couplings of the form $H'^2 \psi_{1,2}^2 / \Lambda$ where Λ is governed by the mass scale of a heavy singlet that mixes with H') [15–17]. More generally, $\delta_{1,2} \ll m_D$ is technically natural as the theory enjoys an enhanced global symmetry (analogous to SM lepton number) when Majorana masses are absent.

then $A' \leftrightarrow \text{SM SM}$ decays and inverse-decays equilibrate the two sectors, seeding an initially large thermal density of dark sector states [26].

A priori, there is no preferred ordering of DM and dark photon masses. However, if $m_{A'} < m_1$ and $e' \gg \epsilon$, then DM freeze-out proceeds predominantly through $\chi_1 \chi_1 \rightarrow A' A'$ annihilation followed by A' decays to visible SM particles. Since this process is s -wave, the CMB limit from Eq. 1 robustly excludes this mass ordering in the sub-GeV mass range.

By contrast, if $m_{A'} > m_1 + m_2$, then DM annihilations to on-shell dark photons are kinematically forbidden, and instead the DM relic density is governed by the coannihilation $\chi_1 \chi_2 \rightarrow \text{SM SM}$, as shown in Fig. 1. In the non-relativistic limit, the cross section for this process is [3, 27]

$$\langle \sigma v \rangle_{\text{ann}} \simeq \frac{16\pi\alpha\alpha'\epsilon^2 m_1^2}{(4m_1^2 - m_{A'}^2)^2}, \quad (9)$$

where α and $\alpha' = e'^2/4\pi$ are the electromagnetic and $U(1)'$ fine-structure constants, respectively. In our calculations, we incorporate all kinematically accessible channels, including hadronic final states, as described in Refs. [28, 29]. Although this cross section is unsuppressed in the low-velocity limit, the CMB bound is alleviated because the χ_2 abundance is thermally depleted before recombination for sufficiently large splittings, thereby shutting off $\chi_1 \chi_2 \rightarrow \text{SM SM}$ at late times. This is discussed in more detail below.

When the temperature of the early Universe cools to $T = T_{\text{fo}} \sim m_1/10$, the total comoving DM density freezes out to a fixed value. Thus, for $\delta \ll m_1/10$, the mass-splitting can be neglected throughout this process, and we follow the calculations of Ref. [3] to determine the initial relic density of $\chi_{1,2}$ particles. In particular, for $\delta \ll m_{1,2} \lesssim 100$ MeV and $m_{A'} \gtrsim \text{few} \times m_1$, the $\chi_{1,2}$ abundance at freeze-out satisfies

$$f_\chi \simeq \left(\frac{0.5}{\alpha'}\right) \left(\frac{10^{-5}}{\epsilon}\right)^2 \left(\frac{m_1}{100 \text{ MeV}}\right)^2 \left(\frac{m_{A'}}{3m_1}\right)^4, \quad (10)$$

where f_χ is the fractional abundance of DM that χ_1 and χ_2 jointly constitute.

Throughout this work, we focus on the parameter space that satisfies the assumptions leading to Eq. 10, fixing to the representative values $m_{A'}/m_1 = 3$ and $\alpha' = 0.5$, and assuming a standard freeze-out cosmology for χ_1 and χ_2 .³ We also fix the value of ϵ by imposing $f_\chi = 1$ such that $\chi_{1,2}$ account for the entire observed DM abundance, unless mentioned otherwise (in Sec. VI we will also investigate DM subcomponents, corresponding to $f_\chi < 1$). In later sections, we vary the

iDM mass-splitting δ to explore a wide range of possible late-time implications of the χ_2 population. However, in the parameter space of interest, it is always the case that $\delta \ll m_1$, so that Eq. 10 is unaffected.

Furthermore, since we always work in the regime where $\delta < m_{A'}, 2m_e$, the decays $\chi_2 \rightarrow \chi_1 A'$ and $\chi_2 \rightarrow \chi_1 e^+ e^-$ are kinematically forbidden and χ_2 is stable on cosmological timescales; we neglect the highly subdominant $\chi_2 \rightarrow \chi_1 + 3\gamma$ and $\chi_2 \rightarrow \chi_1 \nu \bar{\nu}$ decay channels, since the corresponding lifetimes are exponentially longer than the age of the Universe [31].

B. DM – SM Kinetic Decoupling

After DM – SM chemical decoupling, DM – SM scattering $\chi_1 \ell^\pm \leftrightarrow \chi_2 \ell^\pm$ remains in equilibrium due to the large thermal density of SM leptons,⁴ as shown in Fig. 1. These processes do not change the total DM number, but as long as they are in equilibrium, the DM temperature, T_χ , tracks that of the SM, T , such that both approximately evolve inversely with the cosmic scale factor $T_\chi = T \propto a^{-1}$.

Since our focus is on sub-GeV DM, the dominant process that maintains kinetic equilibrium after freeze-out is inelastic scattering off of electrons and positrons, whose abundance vastly exceeds that of any other charged species at temperatures $T \lesssim 100$ MeV. The full thermally-averaged thermalization rate for $\chi_1 e \leftrightarrow \chi_2 e$ is derived in Appendix A, but here we briefly summarize its limiting forms. At both high and low temperatures compared to the electron mass, this rate is well approximated by

$$\Gamma_{\text{kd}} \simeq \frac{8\alpha\alpha'\epsilon^2 T^2}{3m_{A'}^4 m_1} \times \begin{cases} \frac{31}{63} \pi^5 T^4 & (T \gg m_e) \\ \frac{16}{\pi} m_e^4 e^{-m_e/T} & (T \ll m_e) \end{cases}. \quad (11)$$

The DM and SM sectors kinetically decouple from each other at a temperature of $T_\chi = T = T_{\text{kd}}$ when the typical DM particle no longer efficiently transfers momentum with an electron in a Hubble time. This temperature can be approximated by solving $\Gamma_{\text{kd}}(T_{\text{kd}}) = H(T_{\text{kd}})$, where H is the Hubble expansion rate. After this point, the DM temperature no longer tracks that of the SM plasma, instead redshifting more rapidly as an isolated non-relativistic sector with a temperature scaling of $T_\chi \propto a^{-2}$.

For $m_1 \lesssim 1$ GeV and our choice of representative model parameters in Eq. 10, $\Gamma_{\text{kd}} \gg H$ at temperatures comparable to or greater than the electron mass. Thus, $\chi_1 e^\pm \leftrightarrow \chi_2 e^\pm$ scattering steadily depletes the χ_2 population until $T \sim m_e$ when the electron/positron number density

³ Thermal freeze-out models with $m_{A'}/m_1 \lesssim 1$ are typically excluded by measurements of the CMB, as mentioned above, whereas scenarios with $m_{A'}/m_1 \gg 3$ or $\alpha' \ll 1$ are strongly constrained by accelerator searches [3, 30].

⁴ Note that there are also similar interactions with quarks and hadrons, but since their densities are exponentially suppressed at temperatures $T \lesssim 100$ MeV, such interactions are subdominant.

becomes Boltzmann suppressed and the scattering rate falls out of equilibrium. Note that for $m_1 \lesssim 10$ MeV, DM annihilations, as discussed in Sec. III A, decouple after DM – SM scattering, so that $T_{\text{kd}} > T_{\text{fo}}$ and the two earliest processes in Fig. 1 decouple in the opposite order relative to what is shown. In this case, once DM annihilations to the SM freeze out, the temperatures of the two sectors evolve independently. Generally, we expect this to only hold approximately, and we reserve a more careful numerical treatment, involving solving the relevant Boltzmann equations, to future work.

C. DM – DM Chemical Decoupling

DM self-scattering $\chi_1\chi_1 \leftrightarrow \chi_2\chi_2$ (as shown in Fig. 1) is unsuppressed by the small coupling ϵ , and thus can remain in equilibrium long after the processes of the previous two subsections have already decoupled. This implies that even for splittings as small as $\delta \sim \text{eV}$, χ_2 can be thermally depleted well before recombination once $T_\chi \lesssim \delta$.

As derived in Appendix B, the thermally-averaged rate for $\chi_2\chi_2 \rightarrow \chi_1\chi_1$ scattering is given by

$$\Gamma_\chi \simeq \frac{8\pi \alpha'^2 m_1^{3/2}}{m_{A'}^4} n_1 e^{-\delta/T_\chi} \max\left(\frac{\delta}{2}, \frac{T_\chi}{\pi}\right)^{1/2}, \quad (12)$$

where n_1 is the χ_1 number density.⁵ We estimate the DM temperature T_χ^{dec} at which χ_1 and χ_2 chemically decouple from each other by evaluating $\Gamma_\chi(T_\chi^{\text{dec}}) = H$. After decoupling, the primordial abundance of excited states is fixed to

$$f_2 = \frac{n_2}{n_1 + n_2} \simeq \frac{e^{-\delta/T_\chi^{\text{dec}}}}{1 + e^{-\delta/T_\chi^{\text{dec}}}}, \quad (13)$$

where we have used detailed balance to relate the number densities of χ_2 and χ_1 just prior to decoupling, $n_2 \simeq e^{-\delta/T_\chi} n_1$.

D. Primordial Excited Fraction

Using the formalism of Secs. III A, III B, and III C, we determine the total $\chi_{1,2}$ density, temperature evolution, and χ_2 fractional density f_2 , respectively. In Fig. 2, we show f_2 as a function of m_1 and δ . For fixed δ , heavier dark sector masses suppress the rate Γ_χ of Eq. 12, such that $\chi_1 - \chi_2$ interconversion decouples at earlier times, enhancing the relative χ_2 density. On the other hand, for larger splittings, the relative abundance of excited states is increasingly Boltzmann suppressed, yielding smaller values of f_2 . This cosmological value of f_2 is fixed at

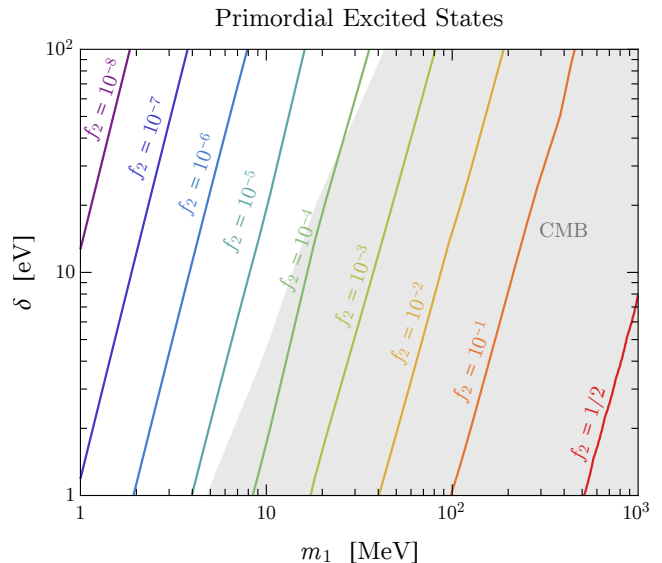


FIG. 2: Contours of fractional χ_2 abundance $f_2 = n_2/(n_1 + n_2)$ set by $\chi_1 - \chi_2$ decoupling in the early Universe, as a function of m_1 and δ . Here, we have fixed $m_{A'}/m_1 = 3$, $\alpha' = 0.5$, and ϵ such that the freeze-out abundance of $\chi_{1,2}$ agrees with the observed DM density. The gray shaded region corresponds to parameter space excluded by CMB annihilation bounds [6].

late times, as shown schematically in Fig. 1 by the lower plateau after $T_\chi = T_\chi^{\text{dec}}$.

This primordial χ_2 fraction governs the rate for $\chi_1\chi_2 \rightarrow \text{SM SM}$ near the time of recombination, which is strongly constrained by CMB data. In particular, Planck bounds such coannihilations to e^+e^- final states according to [6]

$$2f_\chi^2 f_1 f_2 \langle \sigma v \rangle_{\text{ann}} \lesssim 2 \times 10^{-26} \text{ cm}^3 \text{ s}^{-1} \left(\frac{m_1}{30 \text{ GeV}} \right), \quad (14)$$

where the factor of two on the left-hand-side of Eq. 14 accounts for the fact that the limit in Ref. [6] assumed annihilation of self-conjugate DM particles, whereas coannihilations of χ_1 and χ_2 involve distinct species. We have also rescaled the limit by $f_\chi^2 f_1 f_2$, where f_χ from Eq. 10 accounts for the DM fraction that χ_1 and χ_2 jointly constitute, and $f_1 = 1 - f_2$ is the relative χ_1 fraction defined in analogy with f_2 in Eq. 13. Annihilations to muon, tau, and hadronic final states are also similarly constrained, but are weaker by roughly a factor of $\sim 1/3$ due to their smaller efficiency in transferring energy into the intergalactic medium near the time of recombination [5]. The resulting constraint from the CMB is shown in Fig. 2 as the shaded gray region.

IV. GALACTIC POPULATION

After dark sector scattering decouples at T_χ^{dec} , the average cosmological fraction f_2 of the heavier χ_2 state re-

⁵ We note that Eq. 12 agrees with the expressions in Ref. [25], aside from a factor of π discrepancy for $T_\chi \lesssim \delta$.

mains fixed for all subsequent times as the DM temperature continues to fall as a^{-2} due to Hubble expansion. However, in overdense regions where galactic structure forms, the local DM temperature can vastly exceed its average cosmological value due to virialization. Thus, in galaxies and clusters where the local temperature satisfies $T_\chi \gtrsim \delta$, there is an additional late-time population of excited states generated by $\chi_1\chi_1 \rightarrow \chi_2\chi_2$ upscattering, which can exceed the cosmological fraction f_2 computed in the previous section. In this section, we discuss how such a population can arise in the Milky Way.

A. Galactic Model

Since the Galactic χ_2 fraction is exponentially sensitive to the DM velocity, we begin by describing a toy model for the Milky Way. We assume that upon galaxy formation, the χ_2 population has the same cosmological relic fraction f_2 set by dynamics in the early Universe (see Sec. III) and starts off with the same type of Galactic density profile as the χ_1 population.

To simplify our treatment, we approximate the phase-space of DM in the Milky Way as following that of a Maxwell-Boltzmann distribution, with an *effective* temperature T_{mw} that is a function of the galactocentric radius r . In particular, using the virial theorem, we take

$$T_{\text{mw}}(r) = \frac{GM_{\text{enc}}(r)}{3r} m_1, \quad (15)$$

where $M_{\text{enc}}(r)$ is the total mass enclosed within r . M_{enc} is determined directly from our assumed DM density profile as well as the baryonic mass density ρ_B . We approximate the stellar bulge, thin disk, and thick disk contributions to ρ_B from the best-fit spherically-symmetric Hernquist profile model advocated for in Refs. [32, 33],

$$\rho_B(r) = \frac{\rho_{B0} r_0^4}{r(r+r_0)^3}, \quad (16)$$

where $\rho_{B0} = 26 \text{ GeV cm}^{-3}$ and $r_0 = 2.7 \text{ kpc}$.

Later in Sec. V, we will investigate the impact of various choices for the DM density profile. However, for concreteness, in this section we model the initial χ_1 mass density with a Navarro-Frenk-White (NFW) profile [34]

$$\rho_1(r) = \frac{\rho_s}{(r/r_s)(1+r/r_s)^2}, \quad (17)$$

where $r_s = 20 \text{ kpc}$ is the scale radius and ρ_s is normalized to yield a local DM density of 0.4 GeV cm^{-3} at the position of the Solar System, $r = r_\odot \simeq 8.5 \text{ kpc}$.

B. Galactic Evolution

The time-evolution of the Galactic χ_2 population is governed by the Boltzmann equation

$$\frac{\partial \mathcal{F}_2}{\partial t} + \vec{v} \cdot \vec{\nabla} \mathcal{F}_2 + \vec{g} \cdot \frac{\partial \mathcal{F}_2}{\partial \vec{v}} = C[\mathcal{F}_{1,2}], \quad (18)$$

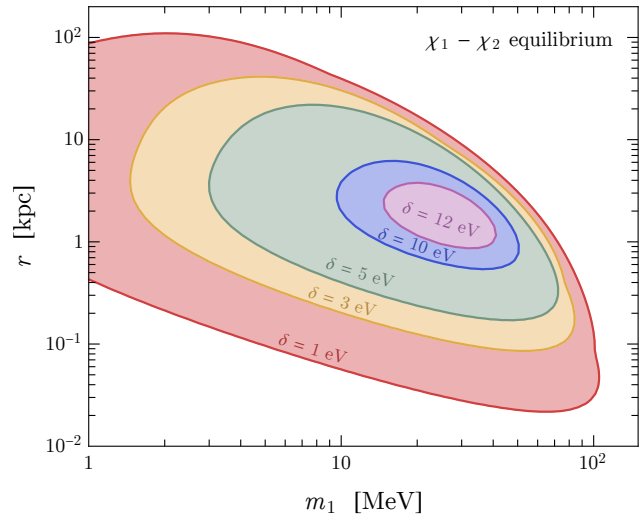


FIG. 3: Radial regions in the Milky Way in which inelastic dark scattering $\chi_1\chi_1 \leftrightarrow \chi_2\chi_2$ reenters equilibrium over the age of the Galaxy $t_{\text{mw}} \simeq 13.5 \text{ Gyr}$, as a function of m_1 and for various representative choices of δ , fixing $m_{A'}/m_1 = 3$ and $\alpha' = 0.5$. We have also assumed an initial NFW profile for χ_1 . For each choice of m_1 and δ , there is a shell of galactocentric radii within which equilibration occurs.

where $\mathcal{F}_{1,2}$ are the phase space densities for $\chi_{1,2}$, \vec{v} is the χ_2 velocity, \vec{g} is the Galactic gravitational acceleration field, and the collision term $C[\mathcal{F}_{1,2}]$ accounts for all $\chi_{1,2}$ scattering processes. Since solving Eq. 18 requires detailed numerical simulations, we simplify the analysis by factorizing the processes of *inelastic* χ_2 production and gravitational evolution, examining upscattering with a simple toy model in this section. Modifications to the $\chi_{1,2}$ distributions due to gravitational dynamics and elastic scattering will be discussed later in Sec. VB, where we consider a wide range of possible scenarios.

We approximate χ_2 production by taking the zeroth moment of Eq. 18 and neglecting gradient and gravitational terms, which amounts to solving

$$\frac{\partial n_2}{\partial t} = n_1^2 \langle \sigma v \rangle_{1 \rightarrow 2} - n_2^2 \langle \sigma v \rangle_{2 \rightarrow 1}, \quad (19)$$

where $n_{1,2}$ is the Galactic number density of $\chi_{1,2}$. Here, the thermally-averaged cross section for $\chi_1\chi_1 \rightarrow \chi_2\chi_2$ upscattering is

$$\langle \sigma v \rangle_{1 \rightarrow 2} = e^{-2\delta/T_{\text{mw}}} \langle \sigma v \rangle_{2 \rightarrow 1}, \quad (20)$$

where $\langle \sigma v \rangle_{2 \rightarrow 1}$ is the thermally-averaged cross section for $\chi_2\chi_2 \rightarrow \chi_1\chi_1$ downscattering. As derived in Appendix B, $\langle \sigma v \rangle_{2 \rightarrow 1}$ is approximately

$$\langle \sigma v \rangle_{2 \rightarrow 1} \simeq \frac{8\pi \alpha'^2 m_1^{3/2}}{m_{A'}^4} \max\left(\frac{\delta}{2}, \frac{T_{\text{mw}}}{\pi}\right)^{1/2}, \quad (21)$$

From Eq. 19, n_2 asymptotes to a constant value once it evolves to $n_2 \simeq e^{-\delta/T_{\text{mw}}} n_1$, as required by detailed balance. In the limit that the initial χ_2 density is small, we can therefore approximate the solution of Eq. 19 as

$$n_2 \simeq n_1 \min(N_{\text{scatt}}, e^{-\delta/T_{\text{mw}}}), \quad (22)$$

where $N_{\text{scatt}} = n_1 \langle \sigma v \rangle_{1 \rightarrow 2} t$ is the number of upscatters per χ_1 particle after time t . Note that χ_2 approaches detailed balance once the average number of upscatters is $N_{\text{scatt}} \sim e^{-\delta/T_{\text{mw}}}$, which occurs on a characteristic timescale of

$$t \sim \frac{e^{\delta/T_{\text{mw}}}}{n_1 \langle \sigma v \rangle_{2 \rightarrow 1}}. \quad (23)$$

Due to its strong temperature dependence, the upscattering cross section $\langle \sigma v \rangle_{1 \rightarrow 2}$ is peaked around a characteristic radial range in the Galaxy, driven by the fact that T_{mw} peaks at intermediate radii. In Fig. 3, we show the radial regions of the Milky Way in which χ_2 reenters chemical equilibrium with χ_1 over the age of the Galaxy, $t_{\text{mw}} \simeq 13.5$ Gyr, as a function of m_1 and for various choices of the splitting δ . We see that for mass-splittings $\delta \lesssim 10$ eV, χ_2 is able to reenter chemical equilibrium over a significant portion of the Galaxy.

We now calculate the Galactic density profile of χ_1 and χ_2 at $t = t_{\text{mw}}$ by numerically solving Eq. 19, along with $n_1 + n_2 = \text{constant}$, at each radius r , starting from the initial condition at $t = 0$ where

$$n_{1,2}(0) = f_{1,2} f_\chi \rho_{\text{DM}} / m_{1,2}, \quad (24)$$

for a given Galactic DM profile ρ_{DM} . Note that this treatment neglects the impact of additional effects, including elastic $\chi_1 \chi_2 \rightarrow \chi_1 \chi_2$ scattering and gravitational dynamics, which will be addressed later in Sec. VB. In Fig. 4, we show the resulting Galactic mass density profile of χ_2 , $\rho_2 = m_2 n_2$, fixing $m_1 = 50$ MeV and $\delta = 5$ eV and for two different assumptions regarding the Galactic evolution of excited states. In particular, for the solid line in Fig. 4, we take χ_2 to be produced along orbits of fixed radius. By contrast, for the dashed line we instead assume that after production, the entire Galactic χ_2 population readjusts to an NFW profile with normalization fixed to conserve the total χ_2 number. These two scenarios are referred to as “unvirialized” and “virialized,” respectively.⁶ For reference, we also show as a dotted line the initial primordial χ_2 profile (see Eq. 24) and as a dot-dashed line a standard NFW DM density profile (scaled down by a factor of two). The peak-like feature near $r \sim 1$ kpc shows the growth to the χ_2 population generated from $\chi_1 \chi_1 \rightarrow \chi_2 \chi_2$ Galactic upscattering at late times. Note that for much larger radii, the distribution does not significantly evolve from its original primordial value since

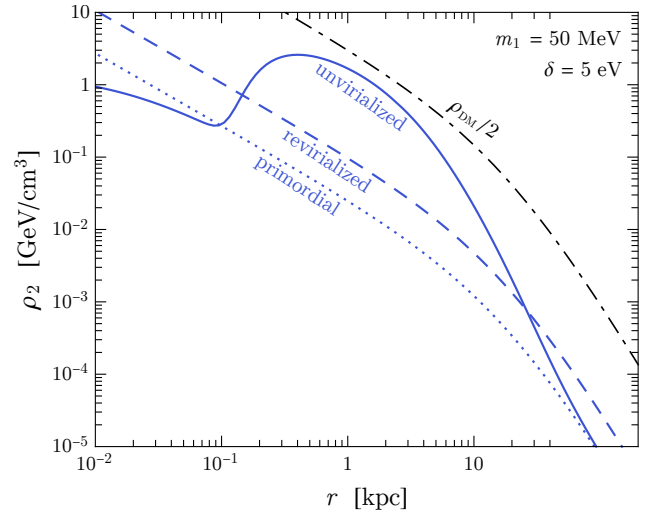


FIG. 4: Radial mass density profiles of χ_2 in the Milky Way, for $m_1 = 50$ MeV, $\delta = 5$ eV, $m_{A'}/m_1 = 3$, $\alpha' = 0.5$, and assuming an initial NFW profile for χ_1 and χ_2 . For the solid line labelled “unvirialized,” we assume that χ_2 remains at the same radius as the progenitor χ_1 particle. For the dashed line labelled “revirialized,” we instead assume that the χ_2 population readjusts to an NFW profile with normalization fixed to conserve particle number. For reference, we also show as a dotted line the initial primordial χ_2 profile (see Eq. 24) and as a dot-dashed line a standard NFW DM density profile, scaled down by a factor of two.

the low density of χ_1 particles suppresses the likelihood to upscatter over the age of the Galaxy. Instead, for much smaller radii, the small Galactic temperature favors downscattering compared to upscattering, reducing the density of excited states in that region.

V. INDIRECT DETECTION

The last section discussed the Galactic density profiles for χ_1 and χ_2 . Here, we use these results to determine the resulting flux of visible particles from DM coannihilations $\chi_1 \chi_2 \rightarrow \text{SM SM}$. We begin by providing some general formalism in Sec. VA. In Sec. VB, we then investigate the sensitivity of our final results to the assumed form of the χ_1 and χ_2 density profiles.

A. General Formalism

In conventional indirect detection studies, the flux Φ_γ of photons from DM annihilations is determined by

$$\frac{d\Phi_\gamma}{dE_\gamma} = c_\chi \frac{\langle \sigma v \rangle_{\text{ann}}}{4\pi m_{\text{DM}}^2} \frac{dN_\gamma}{dE_\gamma} J, \quad (25)$$

⁶ Note that our use of “virialization” is simply meant to imply the process of gravitational relaxation/evolution.

where $\langle\sigma v\rangle_{\text{ann}}$ is the thermally-averaged annihilation cross section in the Galaxy, dN_γ/dE_γ is the number of photons per annihilation event per unit energy E_γ , and the J -factor depends on the Galactic mass density of DM, ρ_{DM} . The constant c_χ incorporates additional factors arising from the counting of DM species. For example, $c_\chi = 1/2$ for Majorana DM in order to not overcount distinct pairs of self-conjugate particles, and $c_\chi = 1/4$ for Dirac DM, since annihilations involve interactions between distinct particles and antiparticles, each of which account for half of the total DM density. For standard DM annihilations, the J -factor is given by

$$J = \int d\Omega d\ell \rho_{\text{DM}}(r)^2, \quad (26)$$

where Ω and ℓ are solid angle and radial coordinates with respect to a local observer, which are related to the galactocentric radial coordinate by

$$r^2 = r_\odot^2 + \ell^2 - 2r_\odot \ell \cos\theta. \quad (27)$$

In our iDM scenario, there are two distinct DM species that coannihilate to yield a flux of SM particles, similar to Dirac DM. However, unlike the Dirac case, the χ_2 population that arises from Galactic upscattering can have a distinct profile, such that we define the J -factor for iDM as

$$J_{\text{iDM}} \equiv \int d\Omega d\ell \rho_1(r) \rho_2(r), \quad (28)$$

where the mass density profiles for χ_1 and χ_2 are determined from Sec. IV B. Note that in the limit where $m_1 \simeq m_2$ and $\rho_1(r) \simeq \rho_2(r) \simeq \rho_{\text{DM}}/2$, $J_{\text{iDM}} \simeq J/4$. With this convention for J_{iDM} , $c_\chi = 1$ for iDM in Eq. 25.

Most indirect detection studies of the Milky Way estimate the reach of various existing or future telescopes by presenting the sensitivity to the annihilation cross section $\langle\sigma v\rangle$, assuming an NFW profile of self-conjugate DM particles. To make direct contact with these studies, we define an *effective* iDM annihilation cross section,

$$\langle\sigma v\rangle_{\text{eff}} \equiv 2 \langle\sigma v\rangle_{\text{ann}} \left(\frac{J_{\text{iDM}}}{J_{\text{NFW}}} \right), \quad (29)$$

where J_{NFW} is defined as in Eq. 26 for an NFW DM profile. The numerical prefactor in Eq. 29 is fixed so that a telescope that is sensitive to self-conjugate (e.g., Majorana) DM annihilations with an NFW density profile and an annihilation cross section of $\langle\sigma v\rangle_{\text{eff}}$ is also sensitive to iDM particles of the same mass and annihilation channels.

B. J -factor Profile-Dependence

Self-scattering processes can lead to significant modifications to the $\chi_{1,2}$ density profiles. For instance, if the χ_2 population is sufficiently abundant, elastic scattering

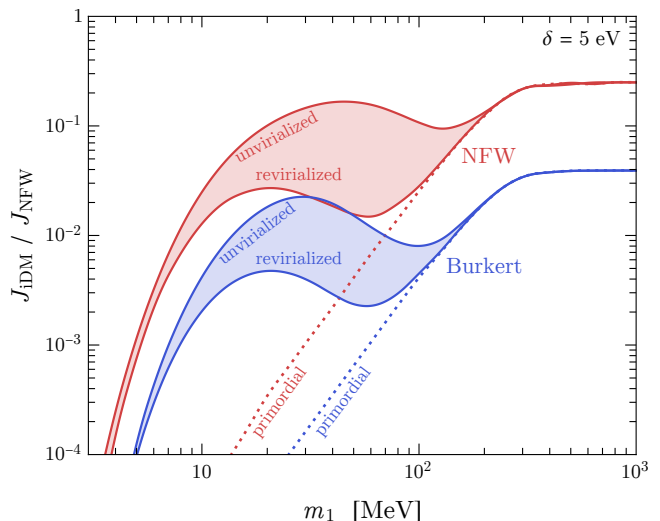


FIG. 5: As solid lines, the Milky Way J -factor for iDM (see Eq. 28) normalized by that of conventional NFW-distributed DM (see below Eq. 29), as a function of m_1 , fixing $\delta = 5$ eV, $m_A/m_1 = 3$, and $\alpha' = 0.5$. We have computed the J -factor by integrating over the polar angles $0^\circ \leq \theta \leq 20^\circ$. $J_{\text{iDM}}/J_{\text{NFW}} = 1/4$ indicates that iDM coannihilations yield the same flux as NFW-distributed Dirac DM annihilating with the same cross section. For the red or blue lines, we assume an initial $\chi_{1,2}$ distribution described by an NFW profile or a 10 kpc core Burkert profile, respectively. The upper boundary of each shaded band labeled “unvirialized” gives the J -factor assuming χ_2 particles maintain the same radius as their χ_1 progenitors, whereas for the lower boundary of each band labeled “revirialized” we assume that the χ_2 population eventually settles into the same type of Galactic distribution as χ_1 with normalization fixed to conserve particle number. Also shown as dotted lines are the contributions from the initial primordial density of excited states, i.e., taking $\rho_{1,2}$ according to their initial values in Eq. 24.

$\chi_1\chi_2 \rightarrow \chi_1\chi_2$ can result in a cored central density, as typically found in models of self-interacting DM (SIDM) [35]. However, the novel upscattering process $\chi_1\chi_1 \rightarrow \chi_2\chi_2$ alters the χ_2 kinematics to counteract such core formation, since it increases the likelihood for such particles to cluster in the inner Galaxy. This is discussed briefly in Appendix C and confirmed in the recent N -body simulation of Ref. [36], which used model parameters comparable to the smallest DM masses and mass-splittings that we consider in this work. Fully modeling all of these effects requires a dedicated N -body simulation in our parameter space of interest, which is beyond the scope of this work. Thus, in this section we approximate the impact of these processes on the iDM J -factor by considering a wide range of possible density profiles.

To determine J_{iDM} , we use ρ_1 and ρ_2 as calculated in

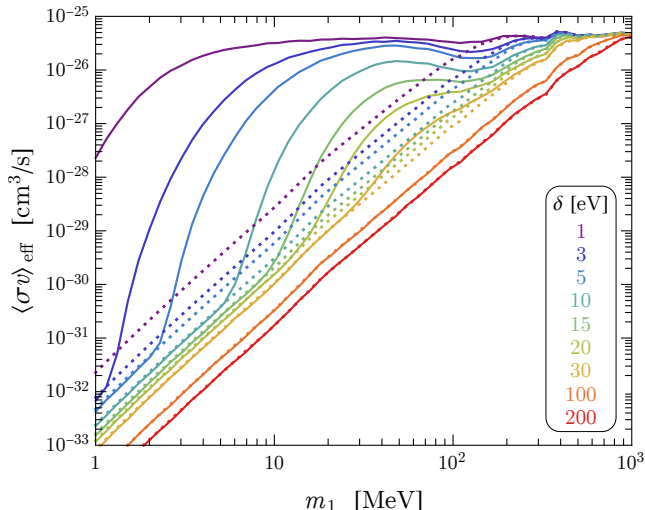


FIG. 6: The effective annihilation cross section $\langle\sigma v\rangle_{\text{eff}}$ (see Eq. 29), as a function of m_1 and for various choices of δ , fixing $m_{A'}/m_1 = 3$, $\alpha' = 0.5$, and ϵ such that the freeze-out abundance of $\chi_{1,2}$ agrees with the observed DM density. The dotted lines show only the contribution from the cosmological relic population of χ_2 parameterized by f_2 in Eq. 13, whereas the solid lines also include the additional contribution from Galactic upscattering in the Milky Way (assuming an initial NFW profile for χ_1 and χ_2 and that the upscattered χ_2 particles stay fixed to the radii at which they are produced).

Sec. IV. Fig. 5 shows the ratio $J_{\text{IDM}}/J_{\text{NFW}}$ as a function of m_1 for $\delta = 5$ eV. Here, we compute the J -factor after integrating over a range of polar angles corresponding to $0^\circ \leq \theta \leq 20^\circ$ and assuming either an initial NFW or Burkert χ_1 profile. In the latter case, the overall flux of the signal is suppressed by our choice of the largest core size typically considered for a Burkert profile, corresponding to ~ 10 kpc [41] (this is meant to illustrate the maximal effect that coring from self-scattering can have on J_{IDM}). Under each of these profile assumptions, we investigate two further possibilities, corresponding to either a χ_2 population that tracks the same radius at which it is produced or instead one that readjusts to the same type as the original χ_1 profile, fixing the normalization to conserve total χ_2 number (see the discussion in Sec. IV). These two choices bracket the range of J_{IDM} values shown in Fig. 5. Also shown as dotted lines are the contributions to the J -factor solely from the initial primordial density of excited states, i.e., taking $\rho_{1,2}$ according to their initial values in Eq. 24. Thus, we see that uncertainties regarding the effects of gravitational dynamics can significantly impact the estimated flux of annihilation products, at the level of a couple orders of magnitude within our parameter space of interest.

In the remainder of this study, we therefore adopt the more optimistic assumptions, corresponding to an initial NFW profile for χ_1 and a population of upscattered χ_2

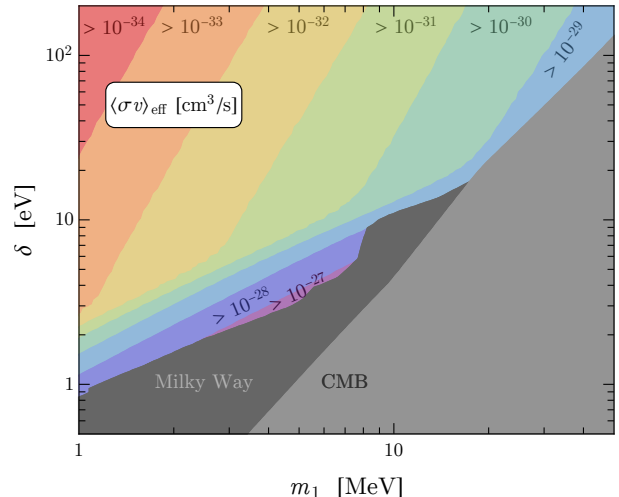


FIG. 7: Contours of the total effective cross section $\langle\sigma v\rangle_{\text{eff}}$ (with contributions from both the primordial and Galactic upscattered χ_2 populations), as a function of m_1 and δ , with the same model assumptions as in Fig. 6. Also shown in gray are regions excluded by observations of the CMB [6] and indirect detection searches of the Milky Way [37–40].

excited states that tracks the radial position of their χ_1 progenitors. However, we note that neither of the bands shown in Fig. 5 take into account that the upscattered χ_2 particles generically have less energy⁷ than their progenitors, which may lead to greater χ_2 densities near the Galactic Center and thereby enhance the J -factor relative to what is shown here. We expand upon this phenomenon briefly in Appendix C and leave a more detailed study to future work.

VI. RESULTS

In Fig. 6, we show $\langle\sigma v\rangle_{\text{eff}}$ (see Eq. 29) as a function of m_1 and for various choices of δ ; the dotted lines show the contribution from only the initial primordial population of excited states. For sufficiently large splittings, upscattering in the Galaxy is exponentially rare, such that the primordial population dominates the flux of coannihilations at late times. From Eq. 20, for a fixed value of δ , upscattering is exponentially suppressed at low masses and power-law suppressed at high masses, resulting in an optimal range of DM masses for the Galactic contribution to $\langle\sigma v\rangle_{\text{eff}}$. On the other hand, for the primordial population, $\langle\sigma v\rangle_{\text{eff}}$ grows with increasing mass due to the

⁷ Although the total energy is conserved in these reactions, the χ_2 produced from upscattering have less combined kinetic and potential energy than their χ_1 progenitors.

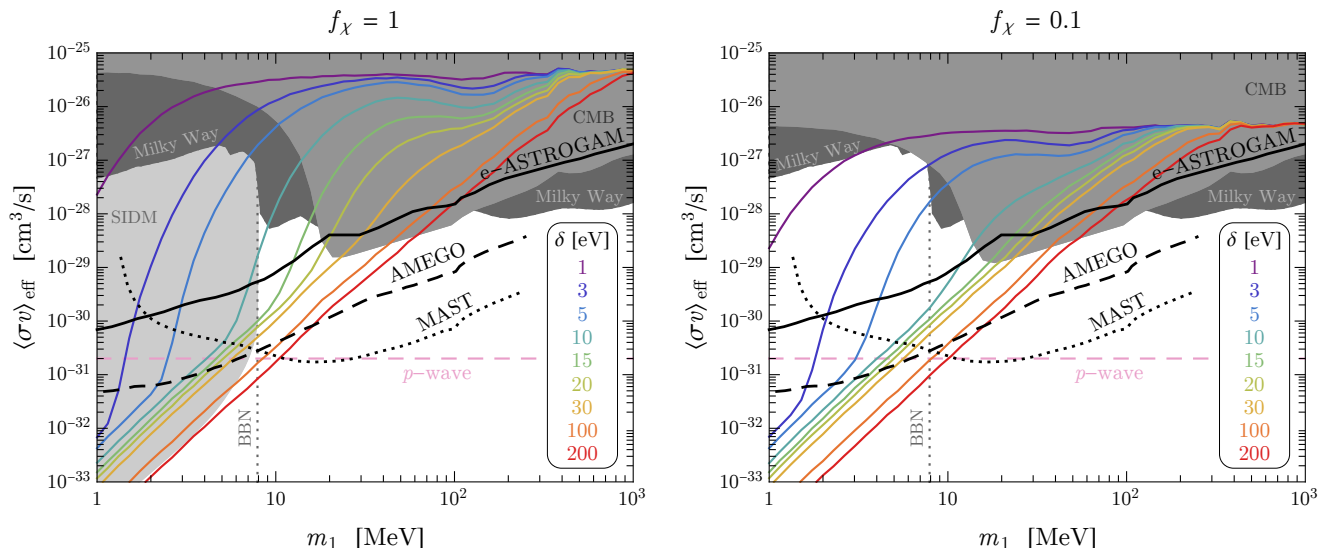


FIG. 8: **Left:** The effective cross section $\langle\sigma v\rangle_{\text{eff}}$ (as in Eq. 29 and Fig. 6), as a function of m_1 for various choices of δ , fixing $m_{A'}/m_1 = 3$, $\alpha' = 0.5$, and ϵ such that the freeze-out abundance of $\chi_{1,2}$ agrees with the observed DM density ($f_\chi = 1$). The initial distributions for χ_1 and χ_2 are taken to be NFW profiles, and we assume that the upscattered χ_2 stay fixed to the radii at which they are produced. Three representative projections of proposed gamma-ray satellites are shown as solid, dashed, and dotted black lines, including e-ASTROGAM [42], AMEGO [43], and MAST [44], respectively. Also shown as shaded gray regions are constraints from the CMB [6], indirect detection searches of the Milky Way [37–40], and DM self-interactions in galaxy clusters (labeled “SIDM”). The lower bound on m_1 , as derived from the successful predictions of BBN under the assumption of a standard cosmology [45], is shown as a vertical gray dotted line. The approximate rate for p -wave annihilating thermal DM is shown as a dashed pink line. Direct detection limits from iDM downscattering constrain splittings larger than those considered here, $\delta \gtrsim 200$ eV [24, 25]. **Right:** Same as the left panel, but instead fixing ϵ such that the freeze-out abundance of $\chi_{1,2}$ constitutes only 10% of the total DM abundance ($f_\chi = 0.1$). In this case, constraints on self-interacting DM do not apply.

enhancement in f_2 (see the discussion in Sec. III D). This is evident in Fig. 6, which shows that for splittings $\delta \lesssim 30$ eV and intermediate masses $m_1 \sim 1$ MeV – 100 MeV, coannihilations arising from the Galactic upscattered χ_2 particles dominantly contribute to $\langle\sigma v\rangle_{\text{eff}}$. Note that for the primordial component, $f_2 \simeq 1/2$ for $m_1 \gtrsim 100$ MeV, such that late-time annihilations are unsuppressed and $\langle\sigma v\rangle_{\text{eff}}$ asymptotes to the standard freeze-out value of $\langle\sigma v\rangle_{\text{eff}} \simeq 5 \times 10^{-26} \text{ cm}^3 \text{ s}^{-1}$ for sub-GeV masses [46].

Fig. 7 displays $\langle\sigma v\rangle_{\text{eff}}$ in the two-dimensional parameter space spanned by m_1 and δ . In light gray we show regions of parameter space excluded by observations of the CMB (as discussed in Sec. III D). Also shown in dark gray are constraints derived from existing observations of the Milky Way. In particular, these consist of limits from gamma-ray observations by INTEGRAL and COMPTEL [37], cosmic-ray measurements by the Voyager 1 spacecraft [38], and X-ray satellites [39, 40]. This region of parameter space corresponds to scenarios in which χ_2 efficiently reenters equilibrium in the Galaxy, thus sourcing an annihilation rate that is comparable to typical s -wave annihilations of thermal DM.

Proposed gamma-ray satellites will be able to significantly extend this sensitivity to larger δ , correspond-

ing to smaller $\langle\sigma v\rangle_{\text{eff}}$. This is evident in Fig. 8, which shows as colored lines the predicted sizes of $\langle\sigma v\rangle_{\text{eff}}$ as a function of mass, for various choices of δ . In the left- and right-panels, we fix $f_\chi = 1$ and $f_\chi = 0.1$, respectively. Also shown as a dashed pink line is the approximate rate for p -wave thermal DM assuming $f_\chi = 1$. Three representative projections of proposed gamma-ray satellites are shown as solid, dashed, and dotted black lines, including e-ASTROGAM [42], AMEGO [43], and MAST [44], respectively. In particular, we have taken the e-ASTROGAM projections from Ref. [13] and the AMEGO and MAST projections from Ref. [14]. We note that Ref. [14] adopted an Einasto DM profile; we have rescaled their projections appropriately to account for the smaller J -factor of an NFW profile. Such instruments have the capability to probe a wide range of currently unexplored thermal iDM parameter space, with annihilation rates orders of magnitude larger than standard p -wave annihilating DM. Although not shown in Fig. 8, the GECCO [47] and COSI [48] instruments may also have competitive sensitivity in this parameter space.

In addition to bounds from the CMB and existing indirect detection searches of the Milky Way, for $f_\chi = 1$ we also display limits from considerations of self-interacting

DM (SIDM). In particular, the large relative DM velocity $v \sim 10^{-2}$ in observed galaxy clusters, such as the Bullet cluster [49], implies that DM as light as $m_1 \sim 1$ MeV has enough kinetic energy to upscatter $\chi_1\chi_1 \rightarrow \chi_2\chi_2$ for splittings as large as $\delta \sim 100$ eV. The region labeled “SIDM” in the left panel of Fig. 8 corresponds to parameter space where upscattering occurs at a rate of $\sigma_{1 \rightarrow 2}/m_1 \gtrsim 10$ cm²/g. In this case, such processes could lead to large deviations in the density profiles of merging galaxy clusters. However, note that since typical studies of SIDM consider elastic scattering, qualitative differences could arise for mass-splittings comparable to the DM kinetic energy, such that properly recasting this bound in the iDM parameter space necessitates a more careful treatment. Moreover, since observations limit the total mass lost in such systems to be less than $\sim 10\%$, iDM self-interactions are completely unconstrained if they make up less than $\sim 10\%$ of the DM [50]. This scenario is considered in the right-panel of Fig. 8, where we instead consider a DM subcomponent with $f_\chi = 0.1$. Also note that in this case, the asymptotic behavior of $\langle\sigma v\rangle_{\text{eff}}$ at high masses following from Eqs. 10 and 29 is given by $\langle\sigma v\rangle_{\text{eff}} \propto f_\chi^2 \langle\sigma v\rangle_{\text{ann}} \propto f_\chi$.

For $m_1 \lesssim 10$ MeV, the thermal density of dark sector particles can alter the expansion rate near temperatures of $T \sim 1$ MeV, leading to predictions for the light element abundances that are in conflict with standard Big Bang nucleosynthesis (BBN). In particular, assuming a standard cosmological history, measurements of the CMB and inferred primordial nuclear abundances exclude $m_1 \lesssim 8$ MeV for the dark sectors considered in this work [45]. This constraint is shown as a dotted gray line in Fig. 8, but can be ameliorated if additional new physics modifies the photon-neutrino temperature ratio or introduces additional relativistic species at early times. We leave a more complete model investigation along these lines to future work.

We conclude this section with a brief discussion on the sensitivity of direct detection searches for DM scattering. In this work, we have refrained from considering mass-splittings larger than $\delta = 200$ eV, since for $200 \text{ eV} \lesssim \delta \lesssim 2m_e$, downscattering of primordial excited states off of electrons, $\chi_2e \rightarrow \chi_1e$, is highly constrained by existing XENON1T, SuperCDMS, and CRESST data [24, 25]. Instead, for $\delta \lesssim 10^{-6} m_1$, upscattering in the form of $\chi_1e \rightarrow \chi_2e$ can be searched for in low-threshold targets, but the limited exposure of current experiments is insufficient to probe the thermal parameter space investigated here [3]. Provided that low-backgrounds can be maintained with larger exposures, future projections for the OSCURA [51] and SuperCDMS [52] experiments could provide sensitivity to such parameter space.

VII. DISCUSSION

We have explored a class of cosmologically-viable DM models in which the same interaction that fixes the relic

abundance also generates MeV-GeV gamma-rays in the Galaxy that are detectable across a wide range of parameter space. In this scenario, visible DM annihilations proceed efficiently in the early Universe through the coannihilation between a lighter χ_1 and heavier χ_2 state, but are exponentially suppressed near the time of recombination as DM self-scattering continues to thermally deplete the χ_2 density. At much later times, the increased kinetic energy of DM particles in the Milky Way enables $\chi_1\chi_1 \rightarrow \chi_2\chi_2$ upscattering to efficiently regenerate a population of long-lived excited states. Their resulting coannihilations give rise to low-energy gamma-rays that are within reach of future telescopes, such as e-ASTROGAM [42], AMEGO [43], and MAST [44]. A novel feature of this scenario is that upscattering, followed by coannihilation, is exponentially-dependent on the DM temperature, which peaks at intermediate radii in the Milky Way. As a result, for certain DM mass-splittings, there exists a radial shell within which χ_1 and χ_2 reenter chemical equilibrium over the age of the Galaxy.

Notably, such theories of inelastic DM serve as an important model-target for accelerator and direct detection searches [1]. Hence, indirect detection may play a key role in enabling model discrimination if signals of sub-GeV DM arise (or fail to arise) elsewhere. For instance, observing a signal in gamma-rays and in low-energy accelerator experiments, such as LDMX [53, 54] or Belle-II [55], would provide evidence in favor of this scenario against other models involving, e.g., p -wave annihilations (as is the case for Majorana fermions or complex scalars annihilating to the SM through an intermediate dark photon [54]).

In regards to direct detection searches, future experiments such as OSCURA [51] and SuperCDMS [52] may ultimately be sensitive to such models, either from downscattering $\chi_2e \rightarrow \chi_1e$ or upscattering $\chi_1e \rightarrow \chi_2e$, depending on the mass-splitting.⁸ Since in such models there is a unique prediction for the relative strength of scattering signals and the Galactic annihilation flux, mutually consistent signals from all three processes would constitute a smoking gun discovery for this scenario and allow the determination of the underlying model parameters.

In addition to what we have investigated in this work, there remain open questions regarding cosmological and astrophysical predictions of these models. Below, we highlight some future directions warranting further study along these lines.

Galactic Dynamics: As noted above, our treatment of $\chi_1\chi_1 \rightarrow \chi_2\chi_2$ Galactic upscattering is based on an

⁸ Note that direct detection projections for inelastic (i.e., pseudo-Dirac) DM often assume that the leading signal arises from loop-induced elastic scattering, which is beyond the reach of upcoming experiments. However, as shown in Refs. [24, 25], downscattering can lead to larger signals, depending on the local density of χ_2 .

analytical model of the Milky Way, which makes several idealized assumptions. To quantify the theoretical uncertainty associated with our modeling, we have considered a wide range of possibilities for the χ_2 distribution in the Galaxy (see Fig. 5). Nevertheless, there are several important effects that cannot be easily estimated using our approach. For example, we separately consider scenarios in which the upscattered χ_2 population either redistributes into the same halo profile as the χ_1 population or, alternatively, tracks the same radius where it was originally produced. However, both possibilities ignore the fact that the χ_2 are less energetic than the χ_1 , due to upscattering. A brief discussion of this point is given in Appendix C. A proper treatment of this effect is beyond the scope of this paper and calls for a dedicated N -body numerical simulation, along the lines of Ref. [36] but geared more towards the specific parameter space investigated in our work. Since including additional χ_2 clustering would likely increase the Galactic J -factor, the analytical projections in this paper are conservative.

Cosmological Evolution: Our calculation of the primordial χ_2 fraction adopts the instantaneous decoupling approximation in which χ_2 number-changing processes ($\chi_1 e \rightarrow \chi_2 e$ and $\chi_1 \chi_1 \rightarrow \chi_2 \chi_2$) maintain chemical equilibrium until their rates fall below the Hubble scale. While this suffices for an order of magnitude estimate of the cosmological χ_2 number density, a more accurate treatment requires numerically solving a system of Boltzmann equations for $\chi_{1,2}$. We leave such an analysis to future work.

Cluster & Dwarf Comparison: For a given mass-splitting, a minimum amount of kinetic energy is required to inelastically upscatter, and thus such processes are highly sensitive to the effective DM temperature. As a result, the types of signals discussed here may vary drastically across astrophysical systems, such as dwarf galaxies and galaxy clusters, whose velocity dispersions differ considerably from that of the Milky Way. In particular, for the parameter space investigated in this work, such signals are exponentially-suppressed in dwarf galaxies due to the smaller DM velocities involved [36, 56]. Conversely, it would be especially interesting to study the sensitivity of proposed low-energy gamma-ray telescopes to signals originating from galaxy clusters [57], as their sizeable velocity dispersions [58] could provide access to models involving much larger mass-splittings. We defer a full treatment of these issues to future work.

ACKNOWLEDGEMENTS

We would like to thank Saniya Heeba, Dan Hooper, Katelin Schutz, and Oren Slone for useful conversations. Fermilab is operated by the Fermi Research Alliance,

LLC under Contract DE-AC02-07CH11359 with the U.S. Department of Energy. This material is based upon work supported by the U.S. Department of Energy, Office of Science, National Quantum Information Science Research Centers, Superconducting Quantum Materials and Systems Center (SQMS) under contract number DE-AC02-07CH11359 and by the Kavli Institute for Cosmological Physics at the University of Chicago through an endowment from the Kavli Foundation and its founder Fred Kavli. This work was completed in part at the Perimeter Institute. Research at Perimeter Institute is supported in part by the Government of Canada through the Department of Innovation, Science and Economic Development Canada and by the Province of Ontario through the Ministry of Colleges and Universities.

Appendix A: DM – SM Kinetic Decoupling

Here, we provide discussion regarding DM – SM scattering and kinetic decoupling. In the limit that $m_{A'} \gg \sqrt{s} \gg \delta$ and $m_1 \gg m_e, T$, the differential cross section for $\chi_2 e \rightarrow \chi_1 e$ is given by

$$\frac{d\sigma_{\chi e}}{dt} \simeq \frac{\pi\alpha\alpha'\epsilon^2}{2m_{A'}^4 m_1^2 p_e^2} \left[2(s - m_1^2 - m_e^2)^2 + 2st + t^2 \right], \quad (\text{A1})$$

where s and t are the usual Mandelstam variables and p_e is the electron momentum. Following Refs. [59, 60], the rate for maintaining kinetic equilibrium is then given by

$$\Gamma_{\text{kd}} \simeq -\frac{1}{3m_1 T} \int \frac{d^3 p_e}{(2\pi)^3} f_e(1 - f_e) v_e \int_{-4p_e^2}^0 dt t \frac{d\sigma_{\chi e}}{dt}, \quad (\text{A2})$$

where $f_e = (e^{E_e/T} + 1)^{-1}$ is the phase-space distribution of electrons with energy E_e , and v_e is the electron velocity. In the limit $T \gg m_e$ or $T \ll m_e$, the above expression reduces to Eq. 11. Note that schematically, the above rate is $\Gamma_{\text{kd}} \sim n_e \sigma_{\chi e} v_e / N_{\text{scatt}}$, where $N_{\text{scatt}} \sim m_1 T / q^2 \gg 1$ is the number of scatters, each exchanging momentum q , needed to transfer a total amount comparable to the DM momentum $\sim \sqrt{m_1 T}$.

Appendix B: DM – DM Chemical Decoupling

Here, we provide more discussion regarding DM downscattering $\chi_2 \chi_2 \rightarrow \chi_1 \chi_1$. To begin, we calculate the cross section in the limit that $m_{A'} \gg \sqrt{s}$ to be

$$\sigma_{2 \rightarrow 1} \simeq \frac{2\pi\alpha'^2}{3sm_{A'}^4} \sqrt{\frac{s - 4m_1^2}{s - 4m_2^2}} \left[7s^2 - 4s(4m_1^2 + 4m_2^2 + 3m_1 m_2) + 76m_1^2 m_2^2 \right]. \quad (\text{B1})$$

To evaluate the thermal average $\langle \sigma v \rangle_{2 \rightarrow 1}$, we use Eq. 3.8 of Ref. [61]. In the limit that $\delta \ll T_\chi \ll m_1$ or $T_\chi \ll \delta \ll m_1$, we arrive at Eq. 21. The corresponding downscattering rate of Eq. 12 is then given by $\Gamma_\chi = n_2 \langle \sigma v \rangle_{2 \rightarrow 1}$, where $n_2 = e^{-\delta/T_\chi} n_1$.

Appendix C: Upscattering in the Milky Way Halo

Since upscattering $\chi_1 \chi_1 \rightarrow \chi_2 \chi_2$ converts kinetic energy into mass energy, it causes particles to fall more deeply into gravitational wells, enhancing the central density of halos, analogous to the dynamics associated with dissipative reactions. This was noted in the detailed numerical simulations of Ref. [36], where it was found that enhanced central densities from upscattering can counteract coring from general scattering-induced heat transport throughout the halo. Here, we provide a brief semi-analytic discussion of the central density enhancement from upscattering, leaving a more dedicated analysis to future work.

We denote the total energy of an initial χ_1 particle as $E = m_1 + T + U$, where T and U are its kinetic and gravitational potential energy, respectively. For convenience, let us rewrite this as $E = m_1 + \tilde{E}$, where $\tilde{E} \equiv T + U$. Using the virial theorem, $T = -\frac{1}{2}U$, we can rewrite \tilde{E} solely in terms of the gravitational energy at radius r ,

$$\tilde{E} = \frac{1}{2} U = -\frac{GM_{\text{enc}}(r) m_1}{2r}, \quad (\text{C1})$$

where $M_{\text{enc}}(r)$ is the total Galactic mass enclosed within r . Using that the total energy E is conserved as χ_1 upscatters and converts into the slightly heavier state χ_2 , we can relate the change in \tilde{E} to the change in mass m_χ of the particle,

$$\frac{d\tilde{E}}{dt} = -\frac{dm_\chi}{dt} = -\Gamma_{1 \rightarrow 2} \delta, \quad (\text{C2})$$

where $\Gamma_{1 \rightarrow 2} = n_1 \langle \sigma v \rangle_{1 \rightarrow 2}$ is the upscattering rate per χ_1 particle. Alternatively, the change in \tilde{E} can be rewritten using the chain rule as

$$\frac{d\tilde{E}}{dt} = \frac{d\tilde{E}}{dr} \frac{dr}{dt} = \frac{GM_{\text{enc}}(r) m_1}{2r^2} \frac{dr}{dt}, \quad (\text{C3})$$

where we used Eq. C1 in the last equality. Equating Eqs. C2 and C3, we have that the change in radius from upscattering is given by

$$\frac{dr}{dt} \simeq -2\Gamma_{1\rightarrow 2} \frac{\delta}{m_1} \frac{r^2}{GM_{\text{enc}}(r)}. \quad (\text{C4})$$

Given a general profile for the enclosed mass $M_{\text{enc}}(r)$ and an initial radius $r_i = r(0)$ at $t = 0$, Eq. C4 can be solved for the radius today $r(t_{\text{mw}})$. This can then be inverted to obtain $r_i(r)$. Since upscattering does not change total particle number, we then relate the initial number density profile at early times $n_i(r_i)$ to the profile today $n(r)$ via $n_i(r_i)r_i^2 = n(r)r^2$. Thus, to leading order in the mass-splitting, the mass density profiles are similarly related $\rho_i(r_i)r_i^2 \simeq \rho(r)r^2$. The final form of the mass density profile is then determined by

$$\rho(r) \simeq \left(\frac{r_i(r)}{r}\right)^2 \rho_i[r_i(r)], \quad (\text{C5})$$

where the function $r_i(r)$ is determined from Eq. C4, as described above. We have found that Eq. C5 accurately captures the salient features found in the “endothermic up-scattering” simulation of Ref. [36]. However, note that the above analysis does not incorporate the full set of dynamics, as it only allows for $\chi_1 \rightarrow \chi_2$ conversion and not the reverse process.

-
- [1] G. Krnjaic *et al.*, “A Snowmass Whitepaper: Dark Matter Production at Intensity-Frontier Experiments,” (2022), [arXiv:2207.00597 \[hep-ph\]](#).
- [2] Rouven Essig *et al.*, “Snowmass2021 Cosmic Frontier: The landscape of low-threshold dark matter direct detection in the next decade,” in *Snowmass 2021* (2022) [arXiv:2203.08297 \[hep-ph\]](#).
- [3] Asher Berlin, Nikita Blinov, Gordan Krnjaic, Philip Schuster, and Natalia Toro, “Dark Matter, Millicharges, Axion and Scalar Particles, Gauge Bosons, and Other New Physics with LDMX,” *Phys. Rev. D* **99**, 075001 (2019), [arXiv:1807.01730 \[hep-ph\]](#).
- [4] Nikhil Padmanabhan and Douglas P. Finkbeiner, “Detecting dark matter annihilation with CMB polarization: Signatures and experimental prospects,” *Phys. Rev. D* **72**, 023508 (2005), [arXiv:astro-ph/0503486](#).
- [5] Tracy R. Slatyer, “Indirect dark matter signatures in the cosmic dark ages. I. Generalizing the bound on s-wave dark matter annihilation from Planck results,” *Phys. Rev. D* **93**, 023527 (2016), [arXiv:1506.03811 \[hep-ph\]](#).
- [6] N. Aghanim *et al.* (Planck), “Planck 2018 results. VI. Cosmological parameters,” *Astron. Astrophys.* **641**, A6 (2020), [Erratum: *Astron. Astrophys.* 652, C4 (2021)], [arXiv:1807.06209 \[astro-ph.CO\]](#).
- [7] Jonathan L. Feng and Jordan Smolinsky, “Impact of a resonance on thermal targets for invisible dark photon searches,” *Phys. Rev. D* **96**, 095022 (2017), [arXiv:1707.03835 \[hep-ph\]](#).
- [8] Elias Bernreuther, Saniya Heeba, and Felix Kahlhoefer, “Resonant sub-GeV Dirac dark matter,” *JCAP* **03**, 040 (2021), [arXiv:2010.14522 \[hep-ph\]](#).
- [9] Nirmalya Brahma, Saniya Heeba, and Katelin Schutz, “Resonant Pseudo-Dirac Dark Matter as a Sub-GeV Thermal Target,” (2023), [arXiv:2308.01960 \[hep-ph\]](#).
- [10] Kim Griest and David Seckel, “Three exceptions in the calculation of relic abundances,” *Phys. Rev. D* **43**, 3191–3203 (1991).
- [11] Raffaele Tito D’Agnolo and Joshua T. Ruderman, “Light Dark Matter from Forbidden Channels,” *Phys. Rev. Lett.* **115**, 061301 (2015), [arXiv:1505.07107 \[hep-ph\]](#).
- [12] Raffaele Tito D’Agnolo, Di Liu, Joshua T. Ruderman, and Po-Jen Wang, “Forbidden dark matter annihilations into Standard Model particles,” *JHEP* **06**, 103 (2021), [arXiv:2012.11766 \[hep-ph\]](#).
- [13] Richard Bartels, Daniele Gaggero, and Christoph Weniger, “Prospects for indirect dark matter searches with MeV photons,” *JCAP* **05**, 001 (2017), [arXiv:1703.02546 \[astro-ph.HE\]](#).
- [14] Adam Coogan, Logan Morrison, and Stefano Profumo, “Precision gamma-ray constraints for sub-GeV dark matter models,” *JCAP* **08**, 044 (2021), [arXiv:2104.06168 \[hep-ph\]](#).
- [15] David Tucker-Smith and Neal Weiner, “Inelastic dark matter,” *Phys. Rev. D* **64**, 043502 (2001), [arXiv:hep-ph/0101138](#).
- [16] Nima Arkani-Hamed, Douglas P. Finkbeiner, Tracy R. Slatyer, and Neal Weiner, “A Theory of Dark Matter,” *Phys. Rev. D* **79**, 015014 (2009), [arXiv:0810.0713 \[hep-ph\]](#).
- [17] Nima Arkani-Hamed and Neal Weiner, “LHC Signals for a SuperUnified Theory of Dark Matter,” *JHEP* **12**, 104 (2008), [arXiv:0810.0714 \[hep-ph\]](#).
- [18] Douglas P. Finkbeiner and Neal Weiner, “Exciting Dark Matter and the INTEGRAL/SPI 511 keV signal,” *Phys. Rev. D* **76**, 083519 (2007), [arXiv:astro-ph/0702587](#).
- [19] Fang Chen, James M. Cline, Anthony Fradette, Andrew R. Frey, and Charles Rabideau, “Exciting dark matter in the galactic center,” *Phys. Rev. D* **81**, 043523 (2010), [arXiv:0911.2222 \[hep-ph\]](#).
- [20] Douglas P. Finkbeiner and Neal Weiner, “X-ray line from exciting dark matter,” *Phys. Rev. D* **94**, 083002 (2016), [arXiv:1402.6671 \[hep-ph\]](#).
- [21] Francesco D’Eramo and Stefano Profumo, “Sub-GeV Dark Matter Shining at Future MeV γ -Ray Telescopes,” *Phys. Rev. Lett.* **121**, 071101 (2018), [arXiv:1806.04745 \[hep-ph\]](#).
- [22] Matthew R. Buckley and Stefano Profumo, “Regenerating a Symmetry in Asymmetric Dark Matter,” *Phys. Rev.*

- Lett.* **108**, 011301 (2012), arXiv:1109.2164 [hep-ph].
- [23] Bob Holdom, “Two U(1)’s and Epsilon Charge Shifts,” *Phys. Lett. B* **166**, 196–198 (1986).
- [24] Masha Baryakhtar, Asher Berlin, Hongwan Liu, and Neal Weiner, “Electromagnetic signals of inelastic dark matter scattering,” *JHEP* **06**, 047 (2022), arXiv:2006.13918 [hep-ph].
- [25] Mariana Carrillo González and Natalia Toro, “Cosmology and signals of light pseudo-Dirac dark matter,” *JHEP* **04**, 060 (2022), arXiv:2108.13422 [hep-ph].
- [26] Jared A. Evans, Stefania Gori, and Jessie Shelton, “Looking for the WIMP Next Door,” *JHEP* **02**, 100 (2018), arXiv:1712.03974 [hep-ph].
- [27] Asher Berlin, Dan Hooper, and Samuel D. McDermott, “Simplified Dark Matter Models for the Galactic Center Gamma-Ray Excess,” *Phys. Rev. D* **89**, 115022 (2014), arXiv:1404.0022 [hep-ph].
- [28] Eder Izaguirre, Gordan Krnjaic, and Brian Shuve, “Discovering Inelastic Thermal-Relic Dark Matter at Colliders,” *Phys. Rev. D* **93**, 063523 (2016), arXiv:1508.03050 [hep-ph].
- [29] Asher Berlin and Felix Kling, “Inelastic Dark Matter at the LHC Lifetime Frontier: ATLAS, CMS, LHCb, CODEX-b, FASER, and MATHUSLA,” *Phys. Rev. D* **99**, 015021 (2019), arXiv:1810.01879 [hep-ph].
- [30] Asher Berlin, Patrick deNiverville, Adam Ritz, Philip Schuster, and Natalia Toro, “Sub-GeV dark matter production at fixed-target experiments,” *Phys. Rev. D* **102**, 095011 (2020), arXiv:2003.03379 [hep-ph].
- [31] Brian Batell, Maxim Pospelov, and Adam Ritz, “Direct Detection of Multi-component Secluded WIMPs,” *Phys. Rev. D* **79**, 115019 (2009), arXiv:0903.3396 [hep-ph].
- [32] Paul J. McMillan, “Mass models of the Milky Way,” *Mon. Not. Roy. Astron. Soc.* **414**, 2446–2457 (2011), arXiv:1102.4340 [astro-ph.GA].
- [33] Manoj Kaplinghat, Ryan E. Keeley, Tim Linden, and Hai-Bo Yu, “Tying Dark Matter to Baryons with Self-interactions,” *Phys. Rev. Lett.* **113**, 021302 (2014), arXiv:1311.6524 [astro-ph.CO].
- [34] Julio F. Navarro, Carlos S. Frenk, and Simon D. M. White, “A Universal density profile from hierarchical clustering,” *Astrophys. J.* **490**, 493–508 (1997), arXiv:astro-ph/9611107.
- [35] Sean Tulin and Hai-Bo Yu, “Dark Matter Self-interactions and Small Scale Structure,” *Phys. Rept.* **730**, 1–57 (2018), arXiv:1705.02358 [hep-ph].
- [36] Stephanie O’Neil *et al.*, “Endothermic self-interacting dark matter in Milky Way-like dark matter haloes,” (2022), 10.1093/mnras/stad1850, arXiv:2210.16328 [astro-ph.GA].
- [37] Rouven Essig, Eric Kuflik, Samuel D. McDermott, Tomer Volansky, and Kathryn M. Zurek, “Constraining Light Dark Matter with Diffuse X-Ray and Gamma-Ray Observations,” *JHEP* **11**, 193 (2013), arXiv:1309.4091 [hep-ph].
- [38] Mathieu Boudaud, Julien Lavalle, and Pierre Salati, “Novel cosmic-ray electron and positron constraints on MeV dark matter particles,” *Phys. Rev. Lett.* **119**, 021103 (2017), arXiv:1612.07698 [astro-ph.HE].
- [39] Marco Cirelli, Nicolao Fornengo, Bradley J. Kavanagh, and Elena Pinetti, “Integral X-ray constraints on sub-GeV Dark Matter,” *Phys. Rev. D* **103**, 063022 (2021), arXiv:2007.11493 [hep-ph].
- [40] Marco Cirelli, Nicolao Fornengo, Jordan Koechler, Elena Pinetti, and Brandon M. Roach, “Putting all the X in one basket: Updated X-ray constraints on sub-GeV Dark Matter,” *JCAP* **07**, 026 (2023), arXiv:2303.08854 [hep-ph].
- [41] Fabrizio Nesti and Paolo Salucci, “The Dark Matter halo of the Milky Way, AD 2013,” *JCAP* **07**, 016 (2013), arXiv:1304.5127 [astro-ph.GA].
- [42] M. Tavani *et al.* (e-ASTROGAM), “Science with e-ASTROGAM: A space mission for MeV–GeV gamma-ray astrophysics,” *JHEAp* **19**, 1–106 (2018), arXiv:1711.01265 [astro-ph.HE].
- [43] Regina Caputo *et al.*, “All-sky Medium Energy Gamma-ray Observatory eXplorer mission concept,” *J. Astron. Telesc. Instrum. Syst.* **8**, 044003 (2022), arXiv:2208.04990 [astro-ph.IM].
- [44] Timur Dzhathoev and Egor Podlesnyi, “Massive Argon Space Telescope (MAST): A concept of heavy time projection chamber for γ -ray astronomy in the 100 MeV–1 TeV energy range,” *Astropart. Phys.* **112**, 1–7 (2019), arXiv:1902.01491 [astro-ph.HE].
- [45] Cara Giovanetti, Mariangela Lisanti, Hongwan Liu, and Joshua T. Ruderman, “Joint Cosmic Microwave Background and Big Bang Nucleosynthesis Constraints on Light Dark Sectors with Dark Radiation,” *Phys. Rev. Lett.* **129**, 021302 (2022), arXiv:2109.03246 [hep-ph].
- [46] Gary Steigman, Basudeb Dasgupta, and John F. Beacom, “Precise Relic WIMP Abundance and its Impact on Searches for Dark Matter Annihilation,” *Phys. Rev. D* **86**, 023506 (2012), arXiv:1204.3622 [hep-ph].
- [47] Elena Orlando *et al.*, “Exploring the MeV sky with a combined coded mask and Compton telescope: the Galactic Explorer with a Coded aperture mask Compton telescope (GECCO),” *JCAP* **07**, 036 (2022), arXiv:2112.07190 [astro-ph.HE].
- [48] Andreas Zoglauer *et al.*, “COSI: From Calibrations and Observations to All-sky Images,” (2021), arXiv:2102.13158 [astro-ph.IM].
- [49] Andrew Robertson, Richard Massey, and Vincent Eke, “What does the Bullet Cluster tell us about self-interacting dark matter?” *Mon. Not. Roy. Astron. Soc.* **465**, 569–587 (2017), arXiv:1605.04307 [astro-ph.CO].
- [50] Maxim Markevitch, A. H. Gonzalez, D. Clowe, A. Vikhlinin, L. David, W. Forman, C. Jones, S. Murray, and W. Tucker, “Direct constraints on the dark matter self-interaction cross-section from the merging galaxy cluster 1E0657-56,” *Astrophys. J.* **606**, 819–824 (2004), arXiv:astro-ph/0309303.
- [51] Oscura Collaboration, “The oscura experiment,” (2022), arXiv:2202.10518 [astro-ph.IM].
- [52] SuperCDMS Collaboration, “A strategy for low-mass dark matter searches with cryogenic detectors in the supercdms snolab facility,” (2023), arXiv:2203.08463 [physics.ins-det].
- [53] Torsten Åkesson *et al.* (LDMX), “Light Dark Matter eXperiment (LDMX),” (2018), arXiv:1808.05219 [hep-ex].
- [54] Asher Berlin and Nikita Blinov, “Thermal Dark Matter Below an MeV,” *Phys. Rev. Lett.* **120**, 021801 (2018), arXiv:1706.07046 [hep-ph].
- [55] Marcello Campajola (Belle-II), “Dark Sector first results at Belle II,” *Phys. Scripta* **96**, 084005 (2021), arXiv:2208.01101 [hep-ex].
- [56] Alan W. McConnachie, “The observed properties of dwarf galaxies in and around the Local Group,” *Astron. J.* **144**, 4 (2012), arXiv:1204.1562 [astro-ph.CO].

- [57] Mariangela Lisanti, Siddharth Mishra-Sharma, Nicholas L. Rodd, and Benjamin R. Safdi, “Search for Dark Matter Annihilation in Galaxy Groups,” *Phys. Rev. Lett.* **120**, 101101 (2018), [arXiv:1708.09385 \[astro-ph.CO\]](#).
- [58] S. Damsted, A. Finoguenov, N. Clerc, I. Davalgaite, C. C. Kirkpatrick, G. A. Mamon, J. Ider Chitham, K. Kiiveri, J. Comparat, and C. Collins, “CODEX: Role of velocity substructure in the scaling relations of galaxy clusters,” (2023), [arXiv:2307.08749 \[astro-ph.CO\]](#).
- [59] Paolo Gondolo, Junji Hisano, and Kenji Kadota, “The Effect of quark interactions on dark matter kinetic decoupling and the mass of the smallest dark halos,” *Phys. Rev. D* **86**, 083523 (2012), [arXiv:1205.1914 \[hep-ph\]](#).
- [60] Bridget Bertoni, Seyda Ipek, David McKeen, and Ann E. Nelson, “Constraints and consequences of reducing small scale structure via large dark matter-neutrino interactions,” *JHEP* **04**, 170 (2015), [arXiv:1412.3113 \[hep-ph\]](#).
- [61] Paolo Gondolo and Graciela Gelmini, “Cosmic abundances of stable particles: Improved analysis,” *Nucl. Phys. B* **360**, 145–179 (1991).